Materials Science & Engineering A 812 (2021) 141056

Contents lists available at ScienceDirect

Materials Science & Engineering A

journal homepage: http://www.elsevier.com/locate/msea

Fabrication of γ-TiAl intermetallic alloy using the twin-wire plasma arc additive manufacturing process: Microstructure evolution and mechanical properties

Lin Wang, Yuelong Zhang, Xueming Hua *, Chen Shen **, Fang Li, Ye Huang, Yuhan Ding

Shanghai Key Lab of Materials Laser Processing and Modification, School of Materials Science and Engineering, Shanghai Jiao Tong University, Shanghai, 200240, China

ARTICLE INFO

Keywords:
Wire arc additive manufacturing
Titanium aluminide
Intermetallic
Plasma arc
Welding

ABSTRACT

Due to the intrinsic high room temperature brittleness and cold-cracking susceptibility, the fabrication and forming of γ-TiAl intermetallic alloy component is extremely difficult. Therefore, in recent years, a wire-arc additive manufacturing (WAAM) technique has been developed to fabricate the γ-TiAl intermetallic alloy by depositing the Ti and Al wires into a single tungsten arc generated molten pool with specific wire feed ratios. However, the WAAM fabricated γ-TiAl intermetallic alloy has been found having inhomogeneous layer-by-layer microstructure and the excessive heat input of tungsten arc would induce significant residual stress in the bulk sample. In the present paper, the previous WAAM has been further upgraded and an innovative twin-wire plasma arc additive manufacturing (TW-PAAM) process has been developed. Afterwards, a γ-TiAl intermetallic alloy wall component with specific chemical composition of Ti-48Al has been fabricated and the metallography, phase composition and tensile properties are characterized subsequently. It has been found that a significantly more uniform microstructure is obtained in the TW-PAAM fabricated γ-TiAl intermetallic alloy than the previous WAAM technique. The content of α_2 phase, lamellar colony size and lamellar spacing exhibited the tendency of decreasing from the lower to upper part along building direction. And the tensile strength and ductility of the lower section are lower than the middle and top sections. In general, the present TW-PAAM technique has shown promising capability of fabricating γ-TiAl intermetallic alloy with lower cost, and the investigation results would become a valuable reference for understanding the evolution mechanism of microstructure and mechanical properties of the additively manufactured TiAl alloy.

1. Introduction

γ-TiAl based alloys have been considered as a promising displacement of Ni-based superalloys for the low pressure turbine (LPT) blades in aero engines, due to the attractive low density and preferential specific strength above 600 °C [1,2]. However, the serious room temperature brittleness induced by its intermetallic nature makes γ-TiAl based alloys difficult to be formed and shaped using conventional methods such as casting, rolling and forging [3,4]. Therefore, in recent years, enormous researches have been conducted to the near-net shaping of γ-TiAl alloys such as high-precision centrifugal casting [4], spark plasma sintering (SPS) [5], electron beam selective melting (EBSM) [6] and the WAAM [7].

As it is known, additive manufacturing (AM) technology builds up near-net shaping components layer-by-layer using the slicing information obtained from the three-dimensional computer aided design (CAD) model [8–10]. To date, by the filler material state, the existing AM processes can be divided into powder-based and wire-feed processes. In the aspect of γ-TiAl alloy AM, most of the research works have been focused on the powder-based AM techniques such as selective laser melting (SLM) [11], laser metal deposition (LMD) [12] and EBSM [13,14]. However, corresponding results have shown that the laser-powder based AM techniques (e.g., SLM, LMD) can hardly build up integrated γ-TiAl bulk sample and easy to generate cold cracking in the deposit [12]. This is because the crack susceptibility of γ-TiAl alloy is very sensitive to the processing cooling rate. Since the laser-powder AM techniques cannot provide adequate interpass temperatures, the cooling rate of the deposition location is too fast thus inducing inevitable cold

* Corresponding author.
** Corresponding author.
E-mail addresses: xmhua@sjtu.edu.cn (X. Hua), cshen486@sjtu.edu.cn (C. Shen).

https://doi.org/10.1016/j.msea.2021.141056
Received 29 October 2020; Received in revised form 8 March 2021; Accepted 9 March 2021
Available online 13 March 2021
0921-5093/

cracking. Although it has been reported that defocusing laser above the deposition plane can preheat the powder particles before they enter the pool, which can reduce the cooling rate to a certain level, but the cracks still cannot completely be prevented [12].

Compared to the laser-based AM techniques, the interpass temperature of EBSM instrument can reach over 1100 °C thus eliminates the cold cracking tendency of the buildup γ-TiAl alloys [14]. Therefore, EBSM is currently the only AM technique capable of near-net shaping γ-TiAl alloy components and being applied in the specific aviation areas [15–17]. However, on the one hand, the extremely high cost and the buildup vacuum chamber size significantly limit the further application promotion of such AM technique [16]. On the other hand, the high vacuum environment and energy input of EBSM can result in high Al evaporation loss (2 at% to 7 at%), which phenomenon in turn affects the microstructure and mechanical properties of the buildup γ-TiAl deposit [18].

In recent years, an innovative WAAM technique has been developed to fabricate the binary intermetallic alloys including Ti-Al [19,20], Fe-Al [21], Ni-Ti [22] and Fe-Ni [23]systems, by feeding dissimilar filler wires independently into a single molten pool generated using a gas tungsten arc welding (GTAW) torch. Compared to the EBSM, the WAAM technique exhibits significantly low equipment and filler material cost, high material deposition efficiency, and the capability of directly reaching full-density in the as-fabricated deposit without expensive post-processing such as hot isostatic pressing (HIP) [9]. However, such tungsten arc WAAM technique is still under its preliminary researching stage, and there are still several intrinsic problems desired to be solved: especially (a) the excessive thermal input and heating area caused by the GTAW troch, which would also induce significant residual stress and substrate distortion [24], and (b) the serious microstructure inhomogeneity between GTAW layer deposits, which would be harmful to mechanical properties [20]. To overcome these two shortcomings, the key is to find a more appropriate deposition power source, which possesses higher deposition energy concentration density and penetration. Therefore, in this case the plasma arc torch of the plasma arc welding (PAW) can satisfy such desire.

As it is known, compared to the GTAW process, although the PAW torch also uses the tungsten tip as the non-consumable electrode, the special designed PAW torch cover compresses the plasma arc during the deposition thus effectively increases the energy concentration density and penetration [25]. Also, since the plasma arc of PAW is initially generated between the tungsten tip and the PAW torch cover rather than the deposition base material, the thermal input of the arc generation process is considerably reduced compared to GTAW process, thus the residual stress and the cracking tendency at the deposition beginning section can be reduced at the same time [25,26]. Besides, the thermal input advantage, the PAW is also capable of producing finer and more uniform microstructures in the deposited metal [26]. In the molten pool of PAW, due to the higher energy concentration density, stronger convection is generated in the molten metal. Therefore, the different alloying elements can be better mixed thus generate more homogeneous microstructure and element distribution in the solidified deposit [26]. In the case of the present WAAM of γ-TiAl alloys, the Ti and Al wires are fed into the molten pool by the independent wire feeders with certain wire feed ratio to generate target γ-TiAl alloy composition, thus the good mixing homogeneity of the pool molten is certainly essential to the success of the target γ-TiAl alloy fabrication and buildup. Considering that the inhomogeneous Ti-Al mixing would possibly generate macro segregation phenomenon, which would cause easily structural failures of the γ-TiAl alloys. The use of PAW torch is promising of producing preferential microstructures in the γ-TiAl deposit. Therefore, in the present research, the TW-PAAM process is developed by changing the previous GTAW power into the PAW to seek more homogeneous microstructure in the buildup γ-TiAl deposit than the previous GTAW based WAAM technique.

Besides the process power source upgrade of the TW-PAAM, the corresponding microstructure and mechanical property variation is also investigated in the present study. It is known that due to the layer-by-layer deposition characteristic of the AM process, the as-deposited metal could be reheated to different phase regions and then cooled rapidly multiple times, resulting in complex microstructure and phase compositions. According to the literatures, no matter what power source is used (laser, electron beam, electric arc, etc.), the microstructure of the AM γ-TiAl alloy performs obvious layer-by-layer distribution along the buildup direction [27–29]. In the case of the WAAM γ-TiAl, the microstructure mainly exhibits full-lamellar grains along the buildup direction, with dendritic grains in the layer bands and equiaxed grains in the layer colony. Such heterogeneous microstructure leads to considerable difference between the tensile properties along the longitudinal and normal directions. Because the thermal cycle times and cooling rates in the specific deposition locations are different along the buildup direction, especially in the WAAM process of which the heat input from the GTAW power source is excessive, thus would cause obvious microstructure change of the WAAM buildup γ-TiAl alloys [20]. Therefore, the investigation of the corresponding thermal cycles on the microstructure and tensile properties of the buildup γ-TiAl alloys is necessary for the further development of the TW-PAAM technique itself.

The purpose of the present research is two-folds: first is to upgrade the power source of the initial twin-wire WAAM process for intermetallic fabrication to the PAW plasma of TW-PAAM process, thus to test and verify the feasibility of using PAW torch as the power source of fabricating the target γ-TiAl alloy; second is to characterize the microstructure and mechanical property variation of the TW-PAAM γ-TiAl buildup component along building direction, thus to provide necessary experimental data for the further development of the TW-PAAM γ-TiAl alloy fabrication technique.

2. Experimental procedures

2.1. TW-PAAM system buildup

The Ti-48Al alloy (at. %) deposition wall was produced by the TW-PAAM. The detailed TW-PAAM buildup parameters are listed in Table 1. During the TW-PAAW process, the pure titanium plate with 5 mm thickness was selected as deposition substrate to exclude other elements besides Ti and Al elements diluting from substrate into the buildup component. The schematic drawing of the TW-PAAW system is shown in Fig. 1(a). Two commercial welding wires of Φ0.8 mm pure titanium (ER TA2) and Φ0.8 mm pure aluminum (ER 1100) were independently fed into the single molten pool using two wire feeders at the wire-feeding rate of 1070 mm/min and 930 mm/min, respectively. The molten pool was formed by a plasma arc welding (PAW) system with a matching Φ 4.8 mm tungsten non-consumable electrode at the deposition current of 90 A and arc length of 8 mm. The plasma gas (0.2 L/min) and inert shielding gas (10 L/min) of the TW-PAAW was 99.999% purity argon. Besides the inert gas of the PAW torch, the shielding gas was also infused to the process from the trailing shielding

Table 1
TW-PAAM parameters for the Ti-48Al alloy buildup wall component.

Parameters	Unit	Value
Deposition current	A	90
Arc length	mm	8
Electrode diameter	mm	4.8
Ti wire-feeding rate	mm/min	1070
Al wire-feeding rate	mm/min	930
Travel speed	mm/min	120
Layer height	mm	1
Buildup wall width	mm	8
Plasma gas flow rate	L/min	0.2
Gas flow rate (torch)	L/min	10
Gas flow rate (cover)	L/min	15
Interpass temperature	°C	500

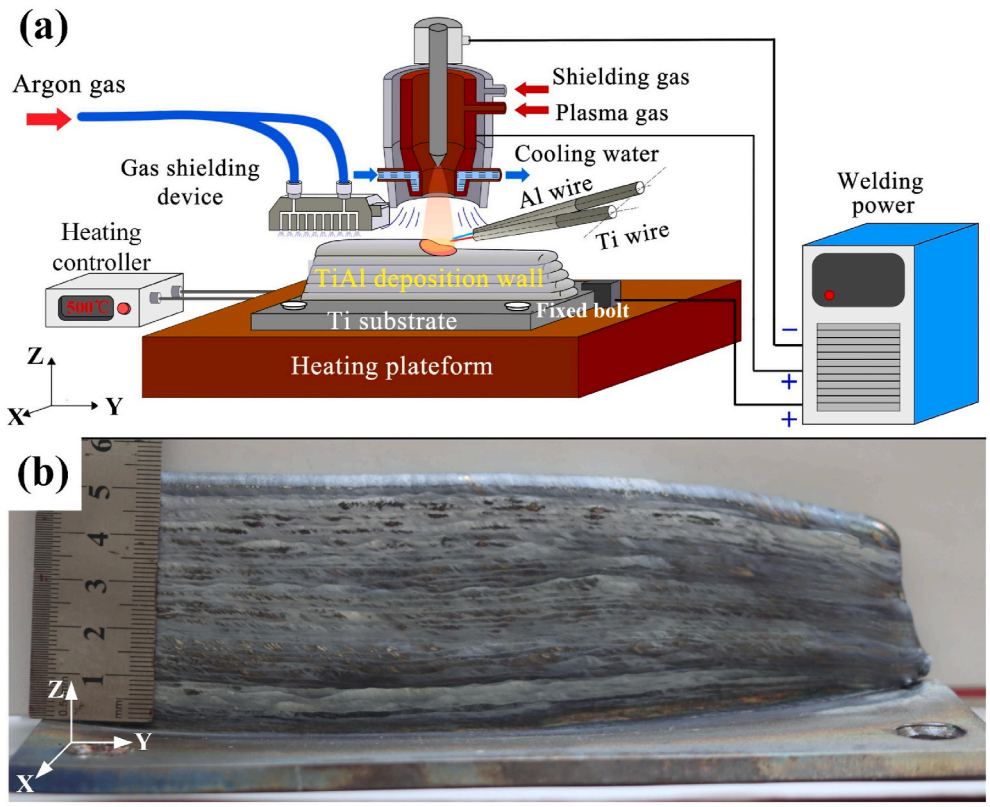

Fig. 1. (a) The schematic diagram of TW-PAAM process, (b) deposited TiAl alloy sample.

cover at the flow rate of 15 L/min. The purpose of the trailing gas shielding cover was to ensure the inert gas environment around the solidified metal at high temperature, thus the excessive oxidation of the γ-TiAl deposition layer can be effectively prevented. In order to prevent the crack of TiAl alloy buildup component, the heating device was used in TW-PAAW system, the interpass temperature was set over 500 °C. During the deposition process, the PAW torch travel speed was 120 mm/min, the single layer height and width were kept at 1 mm and 8 mm,

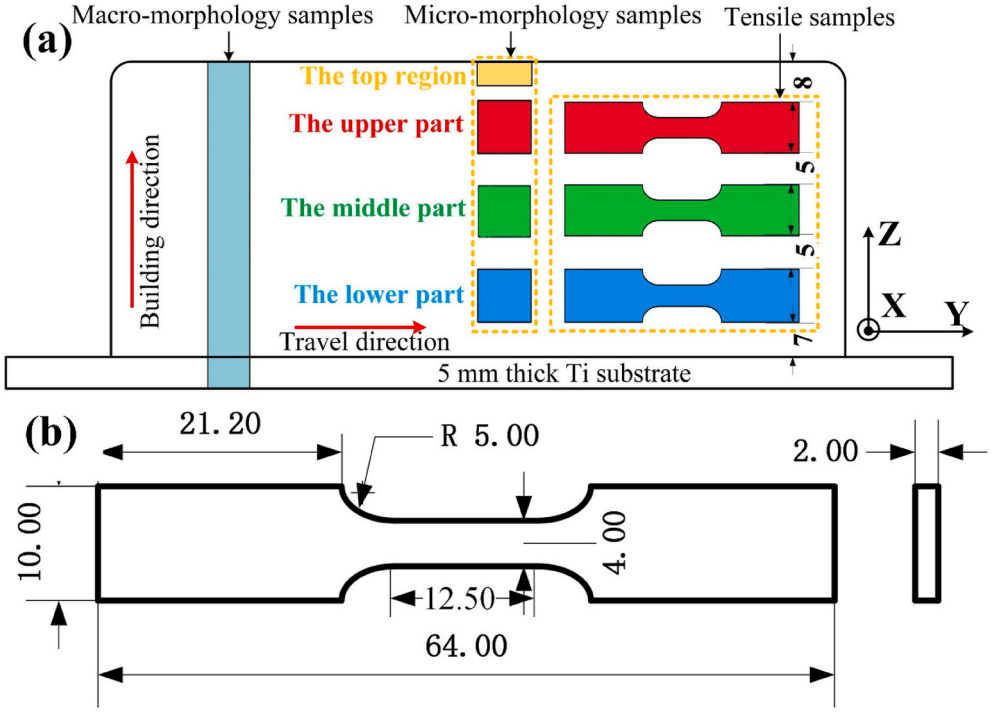

Fig. 2. The schematic of sampling location and dimension of tensile specimens: (a) sampling location for material characterization, (b) dimension of tensile specimen, the unit is millimeter.

respectively. Finally, the buildup wall component with 55 deposition layers reached 55 mm height, as shown in Fig. 1(b).

2.2. Material characterization

The required specimens for microstructure characterizations were obtained from deposited wall using electrical discharge machining (EDM), the specific sampling locations are shown in Fig. 2(a). The metallographic specimens were prepared using standard grinding and polishing preparation methods. The etchant was mixture solution of HF, HNO_3 and H_2O with volume ratio of 2:3:10. The macro metallography was observed by optical microscope (OM, ZEISS Axio Imager A2m). And the microstructure and chemical composition analysis were performed using a scanning electron microscope (SEM, MAIA3 GMU) equipped with energy dispersive X-ray spectrometer (EDS) and backscattering electron (BSE) probe. In order to investigate the grain orientation characteristics of samples at different deposition locations, Electron backscattered diffraction (EBSD) analyses were performed by a NOVA Nano 230 field emission gun scanning electron microscope at 20 kV acceleration voltage, 13 mm working distance and 0.9 μm step size. The sample surface for EBSD observation was mechanically polished down to 0.5 μm, then vibro-polished for 4h. The EBSD data analysis were conducted by using HKL Channel 5 software. The phase composition was identified by a Poly-functional X-Ray Diffractometer (D8 ADVANCE Da Vinci) with a Cu tube radiation at 40 kV and 40 mA, the diffraction angle of 2θ changed from 20° to 100° with step size of 0.02° and a scan rate of 2°/min.

2.3. Mechanical properties test

The Vickers microhardness of buildup wall component (X-Z plane) along building direction was measured at a load of 500 g for 15 s using a Fischerscope HM200 microhardness tester. To investigate the effect of deposition location on the tensile properties of buildup TiAl alloy component, the room temperature tensile properties of as-deposited TiAl alloy at different deposition location were tested using Zwick Roell test system equipped with extensometer at a strain rate of 0.05 s^{-1}. The sampling locations and geometry dimension of tensile specimens are shown in Fig. 2(b). The gauge section of the tensile specimen was 12.5 × 4 × 2 mm. To eliminate the influence of surface roughness, all tensile specimens were processed using the standard grinding and polishing methods before tensile tests. Three tensile samples for each deposition location were tested at least. After the tensile test, the morphology of fractures were analyzed using SEM.

3. Results

3.1. Phase composition

Fig. 3 shows the XRD patterns of the TW-PAAM-fabricated TiAl alloy samples (the upper, middle and lower part). Apparently, the diffraction peaks related to the α_2-Ti_3Al and γ-TiAl phases are detected, no other phase is found, suggesting that the Ti-48Al alloy produced by TW-PAAM consists of α_2 and γ phases regardless of the deposited position. The diffraction peak intensity in the XRD pattern depends on the phase content [30]. As shown in the XRD patterns, the strong diffraction peak corresponding to (111) γ is identified as the main phase. In addition, with the rise of deposition location along the building direction, the intensities of (111) γ and (202) γ diffraction peak increase significantly while the intensities of other γ peaks basically keep unchanged. Meanwhile, the intensities of the (200) α_2 diffraction peak decreases obviously until that at the upper part disappears, while the (201) α_2 peak intensity basically remain consistent. Therefore, the content of γ phase increase while that of the α_2 phase decrease with the increase of the deposition location along the building direction. To further characterize the phase content, a semi-quantitative calculation of the XRD diffraction

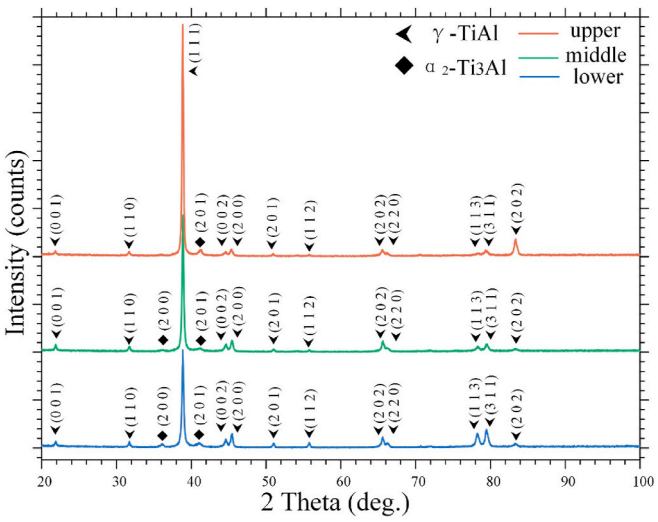

Fig. 3. The X-ray diffraction patterns in X-Z plane of as-deposited TiAl alloy at different deposition location.

pattern is performed using the analysis software. The results show that the volume fraction of α_2 phase are 13%, 10% and 9% at the lower, middle and upper part of buildup TiAl alloy component, respectively, which are in good agreement with the diffraction peaks characteristic analysis.

3.2. Material characterization

The typical microstructure of cross-section (X-Z plane) of the as-deposited specimen are shown in Fig. 4. No crack and gas pore defects are observed in the cross-section, indicating that the TiAl alloy fabricated by TW-PAAM is a full-density component. The microstructure exhibits columnar dendrite morphology along building direction. The alternative stack of two layers with different characteristic are also observed in Fig. 4(a). The observation of the two different layers under the higher magnification, about 1 mm thickness along Z direction, are shown in Fig. 4(c)–(e), one is dendritic morphology composed of lamellar microstructure with interdendritic phase, and the other is composed of fully lamellar colonies consisting of α_2 and γ phase with different colony sizes. The two layers are referred to as dendritic grain region and fully lamellar colony region, respectively. The total thickness of two layers is approximately equal to the layer thickness of each deposition track during the process of TW-PAAM. Therefore, the alternatively distributed layer-like microstructure is closely related to the layer-by-layer deposition mode. Also, it is worth noting that the top region of as-deposited specimen presents dendritic grain microstructure about 3 mm thickness with interdendritic phase, no fully lamellar colony region is observed in the top region within the 3 mm range, as shown in Fig. 4(a)-4(b).

The EDS mapping results of dendritic grain region in different locations along building direction are shown in Fig. 5, it can be seen that the Al enrichment in interdendritic phase is detected, which can be attributed to the Al element segregation during solidification. Combined with XRD results, it can be inferred that the interdendritic phase should be γ phase. The EDS mapping results also show that the extent of interdendritic Al element segregation gradually weaken from the top region to bottom part of as-deposited specimen along building direction. Besides, the EDS point analysis of interdendritic segregations at the top, upper, middle and lower part of as-deposited TiAl alloy are carried out, and shown in Table 2, the Al element segregation degree gradually decreases from the top region to the lower part along buildup direction, which are consistent with the EDS mappings. The microstructure of fully lamellar colony region in different deposition locations are shown in Fig. 6. The

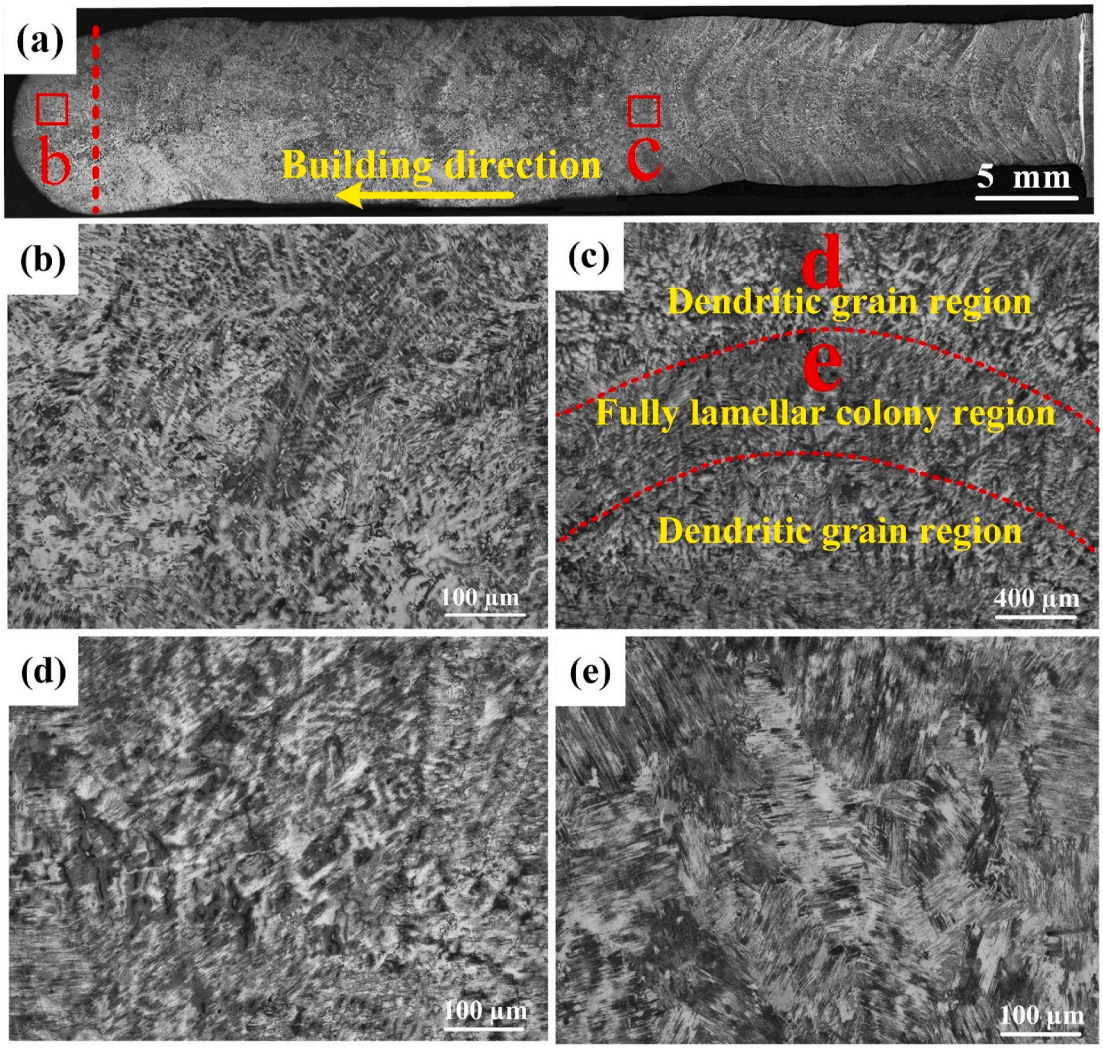

Fig. 4. The macrostructure and microstructure of cross-section (X-Z plane) of TiAl alloy fabricated by TW-PAAM: (a) overview of macrostructure of cross-section, (b) microstructure of the top region, (c) morphology of alternative stack of two layers, (d) dendritic region in the alternative stack of two layers, (e) fully lamellar colony region in the alternative stack of two layers.

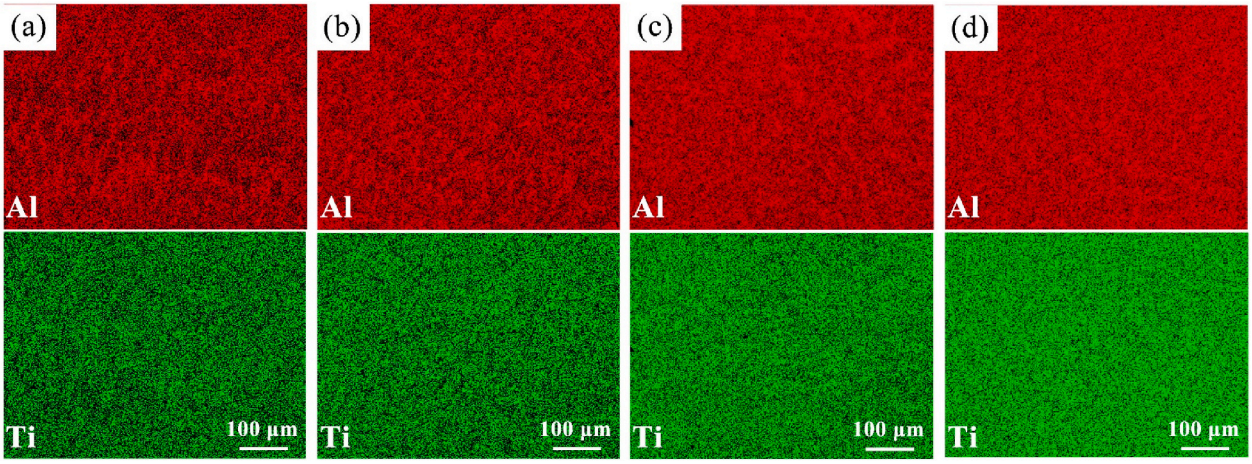

Fig. 5. The EDS mapping results of deposited TiAl alloy at different deposition locations: (a) the top part, (b) the upper part, (c) the middle part, (d) the lower part.

lamellar colony size in the lower, middle and upper part of as-deposited specimen are 256 μm, 233 μm and 168 μm, respectively, exhibiting a decreasing trend from lower to upper part of as-deposited TiAl alloy along buildup direction.

In order to further investigate the microstructural characteristic of TiAl alloy fabricated by TW-PAAM, the BSE is conducted to observe the

Table 2
The EDS point analysis results of interdendritic segregation at different deposition location along buildup direction.

Location	The top region	The upper part	The middle part	The lower part
Ti (at. %)	46.59	48.72	49.94	50.88
Al (at. %)	53.41	51.28	50.06	49.12

microstructure. As shown in Fig. 7, the feathery-like structure, Widmanstätten laths and discontinuous coarsening of lamellae are observed in fully lamellar colony region, which all belong to lamellar structure consisting of α_2 and γ phases. Among them, the Widmanstätten laths are composed of the long straight lamellar packets presenting nearly no misorientation among themselves embedded inside the lamellar colony but with different spatial orientation. Different from Widmanstätten laths, the feathery structures consist of small lamellar lath sets in contact with each other but presenting small spatial misorientations. The volume fraction of α_2 phase in the Widmanstätten lath and feathery

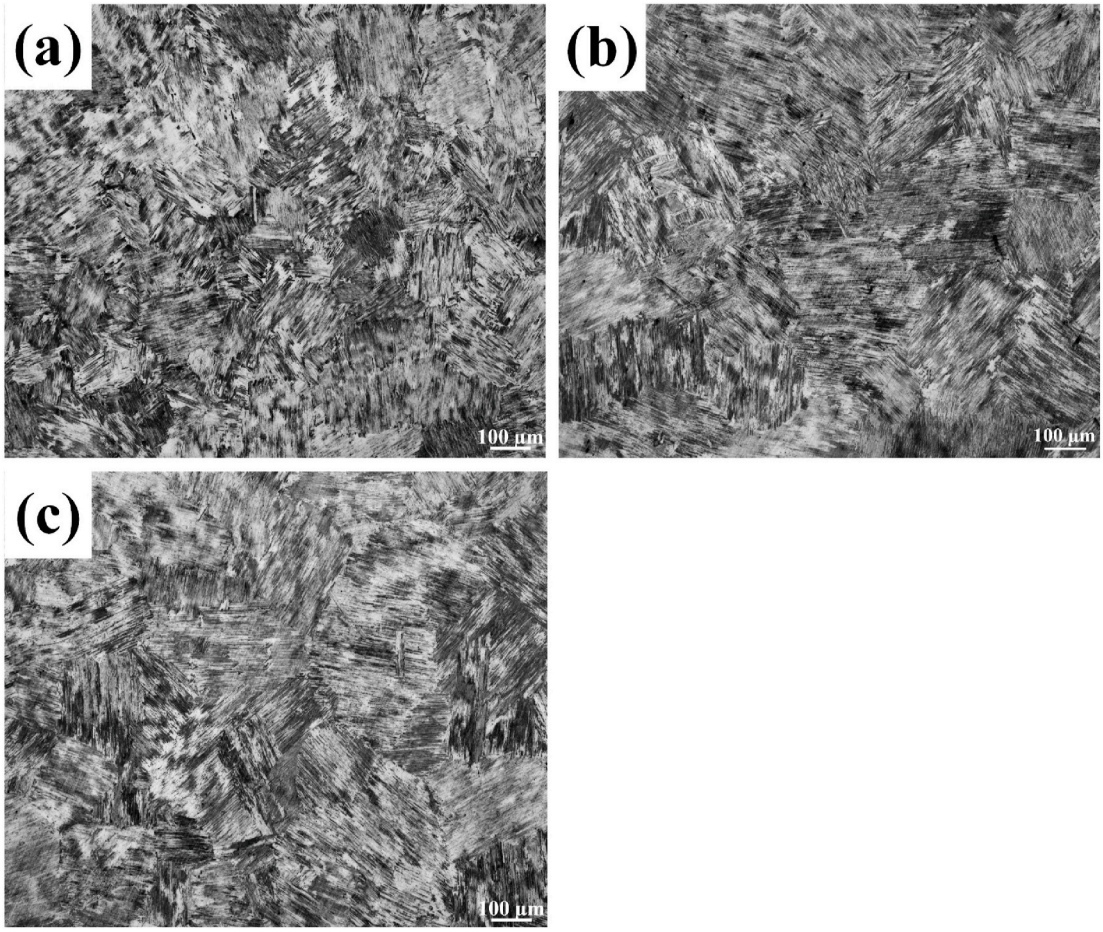

Fig. 6. The lamellar colony microstructure of as-deposited TiAl alloy at different deposition locations: (a) the upper part, (b) the middle part, (c) the lower part.

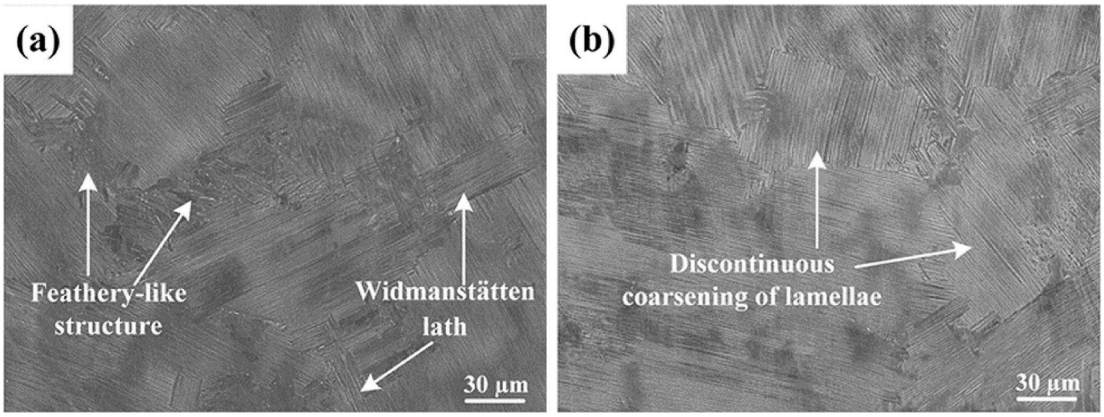

Fig. 7. BSE image in fully lamellar colony region of as-deposited TiAl alloy: (a) feathery-like structure and Widmanstätten laths, (b) discontinuous coarsening of lamellae.

structure is much lower than those in the primary fully lamellar structure, while the orientations of the discontinuous coarsening lamellae are different from the primary lamellae around it. The discontinuous coarsening lamellae contains larger lamellar spacing and lath thickness than the primary fully lamellar structure [31].

Fig. 8 shows the lamellar microstructure of TiAl alloy at different deposition locations along building direction. The results show that the lamellar spacing in the lower, middle, upper and top part of as-deposited specimen are 0.714 μm, 0.556 μm, 0.454 μm and 0.313 μm, respectively, which gradually decrease with the increase of deposition layer along building direction, related to the thermal cycling during the TW-PAAM process.

The EBSD is conducted to investigate the effect of deposition location on crystallographic orientation. The pole figures (PF) of γ and α_2 phase in different deposition locations of as-deposited TiAl alloy are shown in Fig. 9. There are obvious differences of intensity in crystallographic orientation among the different location of as-deposited TiAl alloy samples. The texture intensity can be described by the texture index, and the texture index can be calculated from the orientation distribution function (ODF) f (g) using Eq. (1):

$$\text{Texture Index} = \int (f(g))^2 dg \tag{1}$$

Where *f* is the orientation distribution as a function of the Euler space coordinates *g*, and the *f (g)* is the ODF. The texture index equals to 1 for the isotropic materials, while the texture index of anisotropic materials is larger than 1 [32]. The texture indexes of the γ {111} in upper, middle and lower parts of as-deposited TiAl alloy are calculated to be 3.23, 3.69 and 3.84, respectively, exhibiting no obvious difference and weak texture intensity. The α_2 {0001} crystallographic orientation in different deposition locations along building direction can be observed in Fig. 9. The texture intensities of α_2 {0001} are higher than that of γ {111}, and the middle part of as-deposited TiAl alloy shows a very strong orientation along the α_2 {0001} crystallographic orientation, the texture index is calculated as 25.15, while the texture strength in the lower and upper part exhibit much weaker, their texture indexes are 11.21 and 8.24, respectively.

3.3. Mechanical properties

As described above in Section 3.1, the TiAl alloy fabricated by TW-PAAM exhibits a mixed microstructure along building direction, which would result in change of mechanical properties along the deposition direction. Fig. 10 shows the distribution of microhardness from the near-substrate region to top region along the building direction. It is obvious that the microhardness exhibits significant fluctuation between 281.3HV and 369.4HV, and the microhardness distribution presents approximate periodicity, which is closely related to the microstructural change along building direction. The mean microhardness value reaches 361.1HV in the bottom of deposited TiAl alloy within 2 mm above the substrate surface. The microhardness value of alternatively distributed layers exhibits periodic change with period about 1 mm, which is in accordance with the period of alternatively distributed layer thickness. And the mean microhardness value, about 315HV, is lower in the fully lamellar colony region, while it is higher in the dendritic grain region, about 342HV. The microhardness value keep basically stable, about 320HV, within the top region about 3 mm thickness.

Fig. 11 shows that the tensile stress-strain curves of as-deposited TiAl alloy at different deposition locations along building direction. All stress-strain curves have no obvious yield phenomenon, which is in accordance with that of TiAl alloy components fabricated by other methods. In addition, the results indicate that the deposition location significantly affects the ultimate tensile strength (UTS) and elongation of as-deposited TiAl alloy. The upper part of as-deposited TiAl alloy

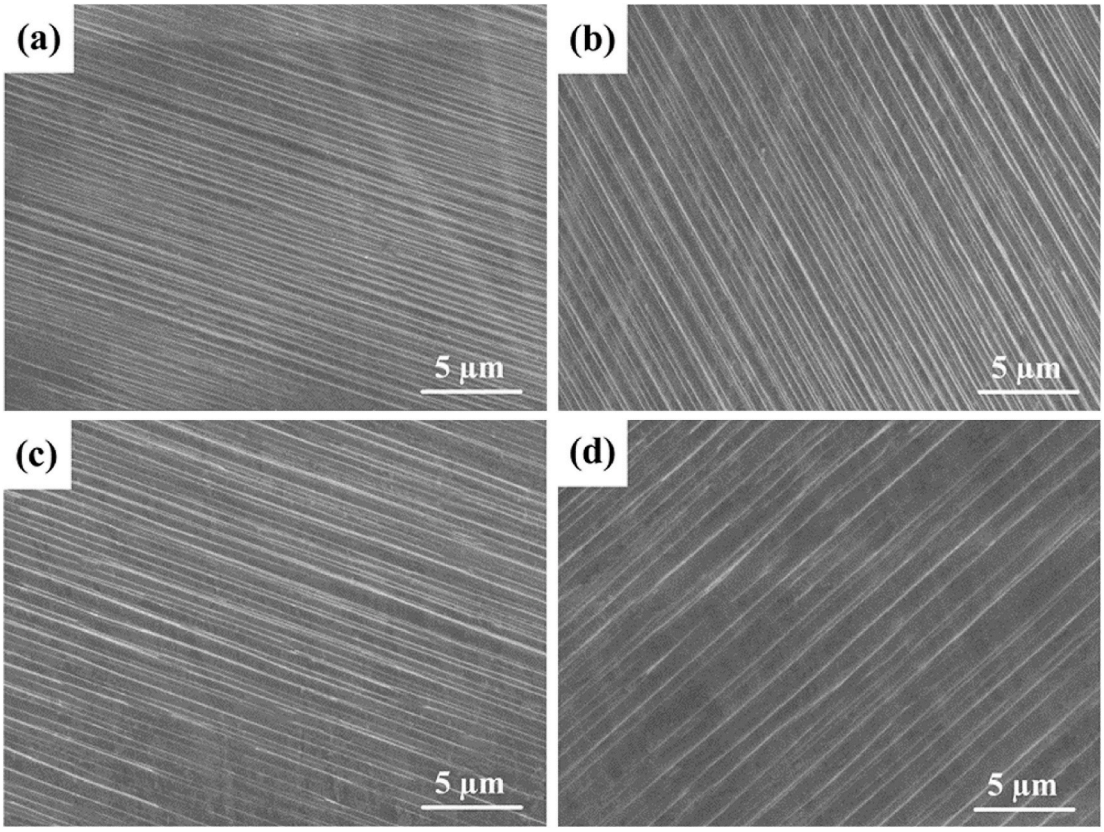

Fig. 8. The BSE images of lamellar morphology of as-deposited TiAl sample at different deposition location: (a) the top part, (b) the upper part, (c) the middle part and (d) the lower part.

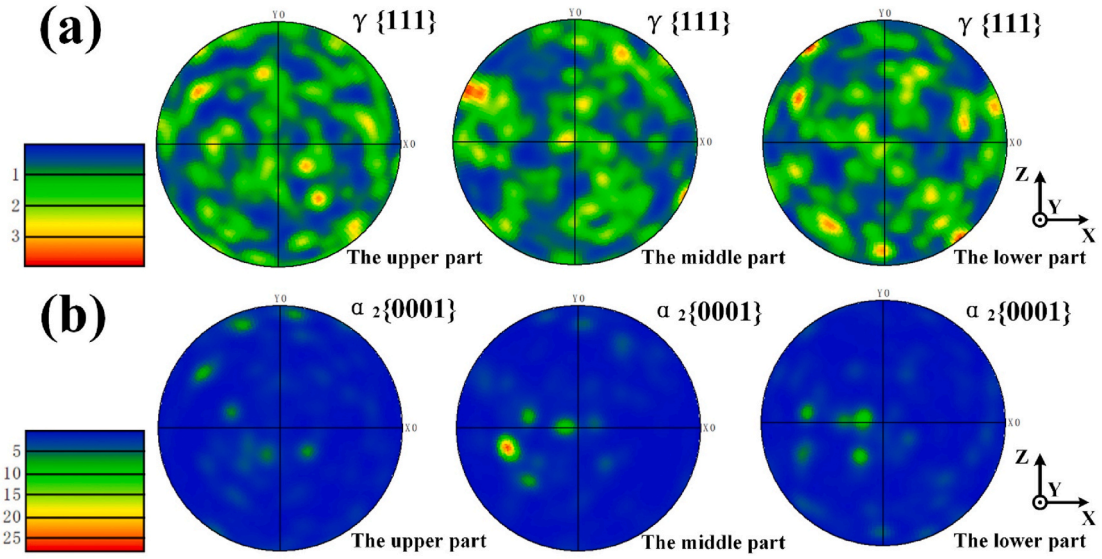

Fig. 9. The pole figures of (a) γ {111} and (b) α_2 {0001} obtained from the as-deposited TiAl alloy at different deposition locations.

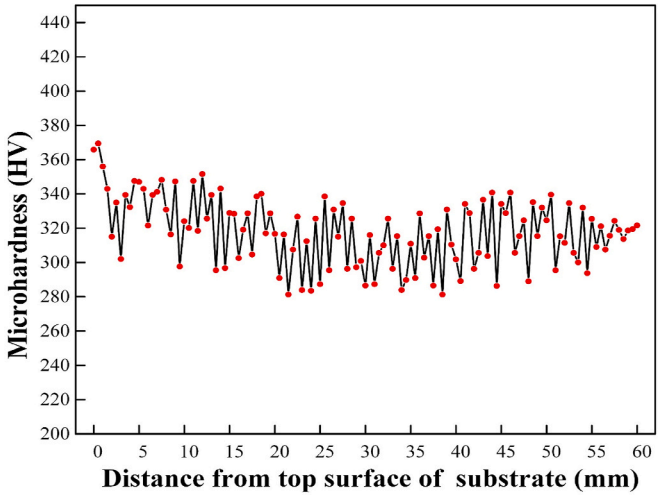

Fig. 10. Microhardness distribution as a function of deposition location along the building direction in cross-section (X–Z).

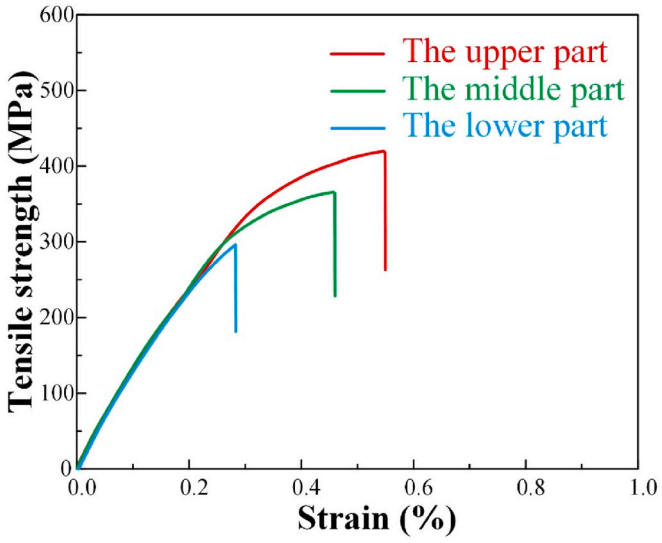

Fig. 11. The influence of deposition location on tensile property of WAAM-produced TiAl alloys at ambient temperature.

exhibits the best comprehensive tensile properties with the maximum ultimate tensile strength and elongation (419.3 MPa and 0.55%), followed by that of the middle part (367.4 MPa and 0.46%). When the tensile tests are conducted to the lower part of as-deposited TiAl alloy, both the UTS and elongation drop significantly to lower value (298.6 MPa, 0.28%). The tensile properties show obvious difference along building direction, which is related to the microstructural characteristic of as-deposited TiAl alloy.

The fracture morphologies of tensile specimens at different deposition locations are analyzed to investigate the tensile fracture mechanism of as-deposited TiAl alloy. According to previous studies [33–35], the TiAl alloys mainly contain two major fracture modes: (1) trans-lamellar fracture mode when the fracture is perpendicular to lamellar microstructure, and (2) inter-lamellar fracture as the cracks propagate along the lamellar interfaces. The fracture morphologies are shown in Fig. 12. The results show that the all fracture surfaces of tensile specimens at different deposition locations contain trans-lamellar fracture characteristics. The facets existed in the fracture surfaces is one of the typical features of inter-lamellar fracture. Some facets can be all observed in the fracture surfaces of three kinds of tensile specimens, but the amount of facets in the upper part of as-deposited TiAl alloy is much smaller than that of the middle part and lower part. In addition, secondary cracks along lamellar interface after tensile test are observed in the fracture surface of lower part.

4. Discussion

4.1. Formation mechanism of the microstructure

The TiAl alloy fabricated by TW-PAAM in the present study exhibits a unique microstructure, which is closely related to the thermal cycling history during deposition.

During the TW-PAAM process, the chemical composition of as-deposited TiAl alloy exhibits no obvious variation along the buildup direction. The solidified microstructure in newly deposited layer epitaxially grow from the former layer since both of them have the same crystal structure. In addition, the microstructure morphology of deposition layer depends on temperature gradient G and solidification rate R, the maximum temperature gradient provides strong driving force for

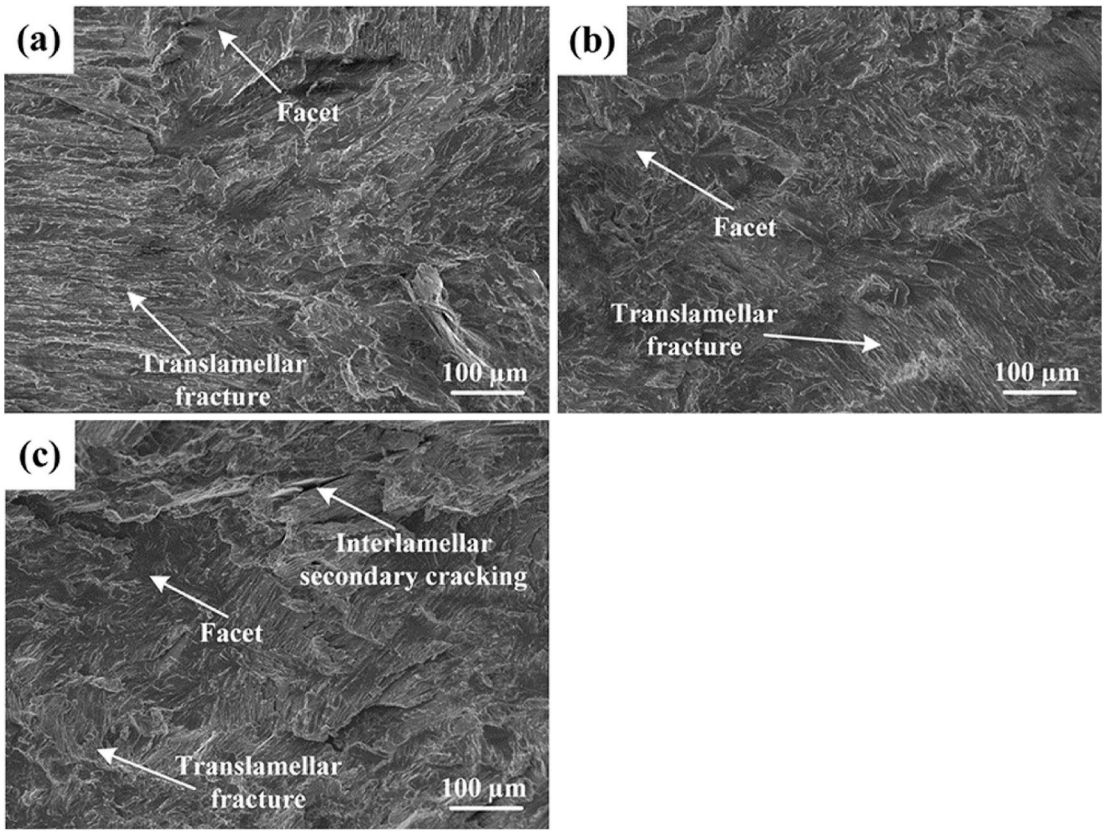

Fig. 12. The fracture surfaces of as-deposited TiAl alloy at different locations after ambient temperature tensile tests: (a) the upper part, (b) the middle part and (c) the lower part.

solidification, so the grain epitaxial growth direction is perpendicular to the curved surface of the solid/liquid interface along the steep thermal gradient, exhibiting the columnar grain characteristic [36].

The TiAl alloy fabricated by TW-PAAM presents the alternatively distributed layer-like microstructure composed of dendritic grain region and fully lamellar colony region. In order to investigate its formation mechanism, the last several deposition layers close to the top region are investigated, especially the last deposition layer without experiencing further thermal cycle, which can therefore reflect primary solidified microstructure of the TiAl alloy fabricated by TW-PAAM. The results show that the as-deposited TiAl alloy in top region within 3 mm exhibits dendritic morphology composed of lamellar microstructure with inter-dendritic Al element segregation, and no fully lamellar colony region is found, which is in non-equilibrium state due to the quick solidification and cooling process.

Fig. 13 shows the Ti-Al binary phase diagram, and the red line represents the solidification path of as-deposited TiAl alloy at 48 at. % Al content. The solidification path of as-deposited TiAl alloy experiences peritectic reaction L + β→α and a eutectic reaction α→α_2 + γ. According to existed reports, it is difficult for the typical eutectic reaction to occur due to the great difference in difficulty extent for nucleation of α_2 and γ phases. Instead of eutectic reaction α→α_2 + γ, the α→α + γ→α_2 + γ occurs to form lamellar structure in the solidification process. Therefore, during the TW-PAAM process, the phase transformation path of TiAl alloy with 48 at. % Al can be summarized as: L→L + β→α→α + γ→α_2 (Ti_3Al) + γ (TiAl). Due to the high cooling rate of PAW, the rate of peritectic reaction L+β→α is much slower, and the α phase is poor in Al element. So the Al element is rich in the interdendritic region, causing interdendritic segregation, finally generates interdendritic γ phase.

According to the literatures, the fully lamellar, nearly lamellar, duplex and nearly gamma microstructure can be obtained depending on the heat treatment at different temperature, as shown in Fig. 13(a)–(d)

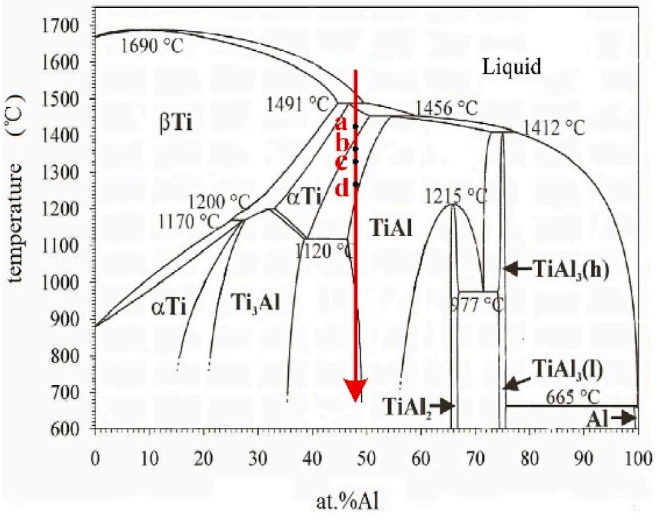

Fig. 13. Ti-Al binary phase diagram, the red arrow represents the solidification path and phase transition of Ti-48Al (at. %) alloy. (For interpretation of the references to colour in this figure legend, the reader is referred to the Web version of this article.)

[2]. During the TW-PAAM, the as-deposited TiAl alloy is reheated to different phase region, which would result in forming different microstructures. The α→γ belongs to the diffusion-type phase transformation, of which the transformation rate is quite slow, while the cooling rate is very fast during the TW-PAAM, and there is no enough time to form nearly lamellar, duplex and nearly gamma microstructure. Therefore, only fully lamellar microstructure is observed in the as-deposited

sample.

As mentioned earlier, the dendritic morphology composed of lamellar microstructure, with about 3 mm thickness, is observed in top region. It is noteworthy that the as-deposited TiAl alloy mainly consists of alternatively distributed dendritic grain region and fully lamellar colony region, and the thickness of repeated two layers is about 1 mm, approximately equal to that of each deposition layer. During the TW-PAAM process, the former deposited layer can be partially remelted, the no remelted area close to the molten pool is heat treated at different temperatures, forming various microstructures. However, the thickness of dendritic grain region in the top region is about 3 mm, which is larger than that of single deposition layer with 1 mm thickness. According to the microstructure characteristics of as-deposited TiAl alloy, the possible solid-state phase transformation during the thermal cycle can be inferred, as shown in Fig. 14. The first thermal cycle represents temperature variation during the solidification, the as-deposited microstructure exhibits dendritic grain morphology consisting of lamellar microstructure with interdendritic γ phase, when the next layer is deposited, the former deposited layer is partially remelted, thus forming dendritic grain microstructure. The unremelted area close to molten pool is reheated to different phase regions. Due to higher cooling rate, the heat treatment time for the deposited layers is limited. Therefore, on the one hand, the nearly lamellar, duplex and nearly γ microstructure are not formed in the area below α transformation temperature (T_α). On the other hand, the fully lamellar colony microstructure is formed by three thermal cycles at temperatures above T_α.

As deposition process continues, the temperature of deposited layers far away from the molten pool gradually decreases below the phase transformation temperature, so the microstructure no longer occurred to change, forming the alternatively distributed layer-like microstructure consisting of dendritic grain region and fully lamellar colony region along buildup direction. However, it is worth noting that the microstructure is not perfectly layer-like along deposition direction, existing some disturbance, some fully lamellar colonies are interrupted by the dendritic grains. This indicates that some other factors, such as element distribution, heat input, etc., can also influence the microstructure characteristic, so the formation mechanism of the entire morphology need to be further investigated.

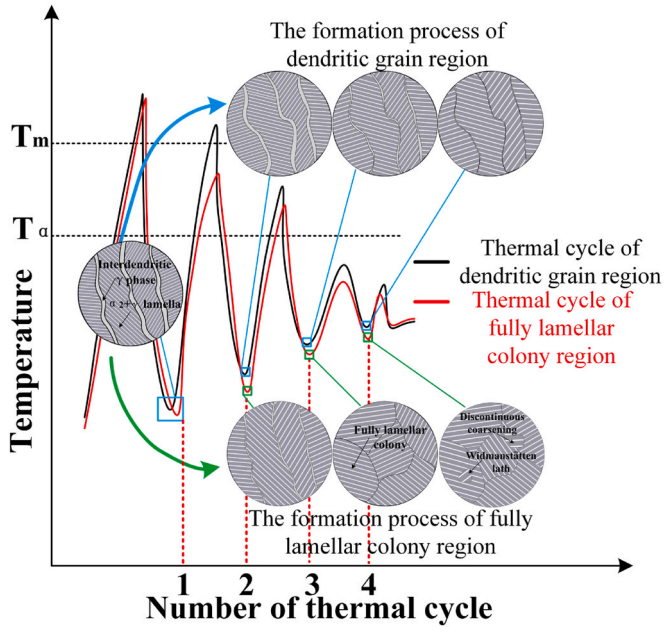

Fig. 14. Evolution of microstructure during thermal cycles(T_m represents the melting point of Ti48Al alloy, T_α represents the phase transformation temperature of α phase).

With the increase of deposition layers, the number of thermal cycles on the as-deposited layer gradually increases from the top to bottom part along the buildup direction. Therefore, the interdendritic segregation is also reduced gradually, which occurs to $\gamma \rightarrow \alpha \rightarrow \alpha_2 + \gamma$ phase transformation during thermal cycle. And the volume fraction of α_2 phase gradually increases from the top region to the lower part. The thermal cycle also influences the lamellar colony size, lamellar spacing and lath width of lamellar microstructure. The total time for lamellar colony and lamellar lath coarsening increases gradually with the number of thermal cycle increasing. So the lamellar colony, lamellar spacing and lath width increase from the top to bottom region along buildup direction.

Apart from the above mentioned microstructure characteristic, some other microstructures, including the feathery structure, Widmanstätten laths and discontinuous coarsening of lamellae, are also observed in the as-deposited TiAl alloy, which are mainly attributed to the complex thermal cycling history during TW-PAAM process. According to previous investigations [31], the volume fraction of α_2 phase is much lower in Widmanstätten laths and feathery structure than primary lamellar structure. The Widmanstätten laths are formed under the intermediate cooling rate by two possible types of nucleation mechanisms [31,37]. One is the primary Widmanstätten lath directly nucleating over the face of the existing γ lamellar structure, basing on an edge-to-face relationship. The other mechanism is a twinning event in the high temperature hexagonal grain induced by cooling, transforming into the first γ Widmanstätten lath. The twin related γ variants in the adjoining γ lamellae offers low interfacial energy, favoring in twin γ/γ interface, so the Widmanstätten lath contains mostly face-to-face γ/γ twin related lateral interfaces. The α_2 phase precipitates subsequently along the interfaces of existed γ laths, forming the Widmanstätten laths microstructure. Fig. 15 (a) shows the schematic map of two formation mechanisms for the Widmanstätten laths, the nucleation mechanism is the only difference between them. During the rapid cooling, the feather-like microstructure are attached to primary lamellar colony boundary, which can extend into the adjoining the α grain without any deviation [38]. The extended lamellaes also grow laterally and nucleate with twin relationship over its lateral side by face-to-face, forming the new laths. With the lamellae growing further into the grain, facing more resistance due to the elastic strain generating, and there are higher elastic strain over its edges. Therefore, the new lamellae with slight misorientation nucleates over the edges of the existing lamellae, exhibiting edge-to-edge orientation relationship. Then the new lamellae starts nucleating over its lateral faces through face-to-face relationship. Finally, the feathery-like structures are formed. The schematic diagram of the formation mechanism for feathery-like microstructure is shown in Fig. 15(b). Besides, the discontinuous coarsening phenomenon is also observed, its formation process is illustrated by Fig. 15(c). The major driving force for discontinuous coarsening is the reduction of interfacial energy and chemical free energy [39]. In addition, the as-deposited microstructure is usually in a non-equilibrium state due to fast cooling rate, which also can offer driving force for discontinuous coarsening. The discontinuous coarsening microstructure exhibits much larger lamellar spacing, which exerts an adverse effect on the mechanical properties.

4.2. Mechanical properties

According to above discussions, the as-deposited TiAl alloy presents mixed microstructure due to multiple thermal cycle, which can exert significant influence on the mechanical properties. Therefore, the microhardness and tensile properties of TiAl alloy at different deposition locations are analyzed.

The microhardness variation of TiAl alloy is closely related to the microstructural characteristics including the lamellar colony size, lamellar spacing and phase category and volume fraction, etc. The microhardness of α_2 phase is higher than that of γ phase [40]. Besides, according to the previous reports, the relationship of the lamellar colony size, lamellar spacing and microhardness can be concluded as [41]:

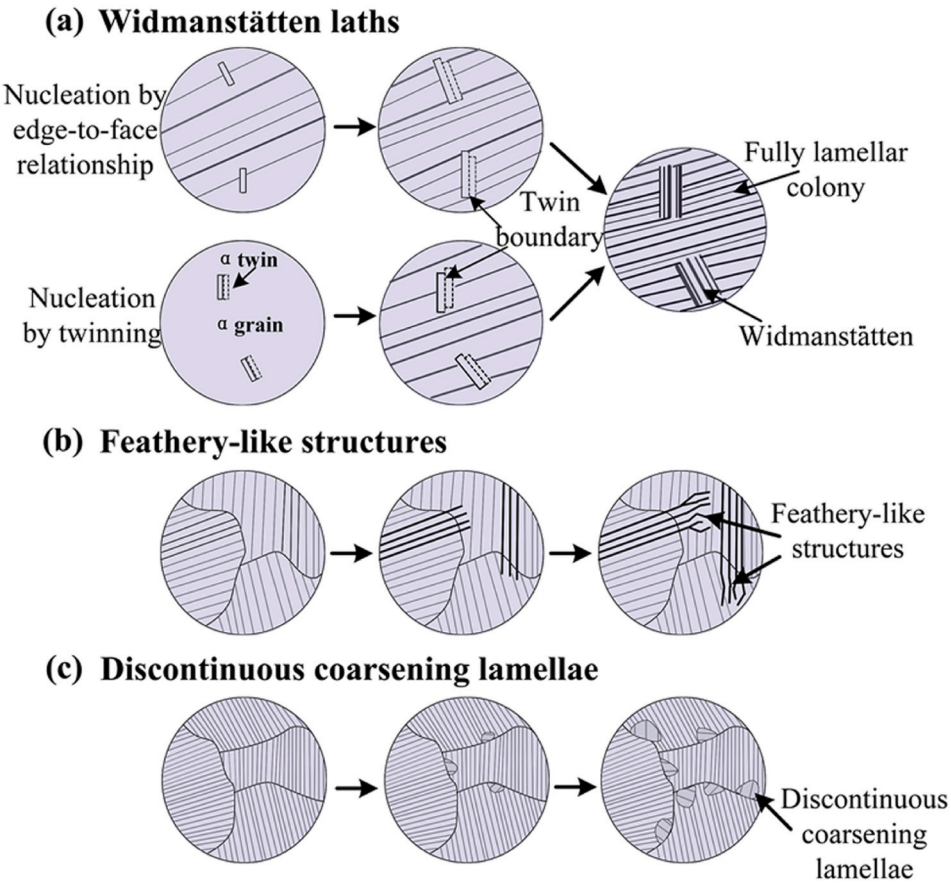

Fig. 15. Schematic profiles of the possible formation process of various microstructures during the deposition process of TiAl alloy fabricated by TW-PAAM [31]: (a) Widmanstätten laths, (b) feathery-like structures and (c) discontinuous coarsening lamellae.

$$H = H_0 + K\lambda^{-0.5} \quad (2)$$

where the H is microhardness, λ is the colony size or lamellar spacing, both H_0 and K are constants. When the lamellar colony size and lamellar spacing are smaller, the ability of inhibiting the dislocations movement is stronger, the microhardness value becomes higher. Therefore, the microhardness value can be increased by decreasing the lamellar colony size and lamellar spacing [42].

The area close to the base metal, with about 2 mm thickness, presents less Al content due to the dilution of Ti substrate partial melting and its cooling rate is much higher. Thus, it contain more α_2 phase and higher residual stress, which help the enhancement of microhardness, finally exhibiting the highest microhardness in the near substrate area. Besides, the microhardness distribution exhibits approximate periodicity along building direction, the period is about 1 mm, approximately equal to that of alternatively distributed layers. The mean microhardness value is much higher in the dendritic grain region (342HV) than that in the fully lamellar colony region (315HV). There are some Widmanstätten laths, feathery structure and discontinuous coarsening structure in fully lamellar colony region, the volume fraction of α_2 phase in these microstructure is lower than that of fully lamellar microstructure, and the discontinuous coarsening structure exhibits larger lamellar spacing, so their microhardness is much lower than that of fully lamellar microstructure. Finally, the dendritic grain region exhibits higher microhardness than fully lamellar colony region. It is worth noting that the mean microhardness value in the lower, middle and upper part is 329.2 HV, 317.5 HV and 328.9 HV, respectively. There is no significant difference in microhardness between the lower part (large amount of α_2 phase, large lamellar colony size and wide lamellar spacing) and the upper part (small amount of α_2 phase, small lamellar colony size and narrow lamellar spacing), while the microhardness of the middle part (middle amount of α_2 phase, lamellar colony size and lamellar spacing) is slightly lower, which is attributed to the synthetic effect of the volume fraction of α_2 phase, lamellar colony size and lamellar spacing. The microhardness value keeps stable in the top region within about 3 mm thickness due to dendritic grain structure without obvious change.

The room temperature tensile properties of TiAl alloy fabricated by TW-PAAM are closely related to the deposition location. The tensile strength and elongation are gradually enhanced from the lower part to the upper part, which is mainly attributed to the variation of microstructure characteristics. According to the previous reports [42,43], the fine colony size and lamellar spacing can improve the tensile properties of TiAl alloys, which can be explained by the interaction between lamellar colony boundary, lamellar interfaces and the dislocations movements. There are more semi-coherent interfaces in TiAl alloy with finer lamellar spacing, inhibiting the dislocations movements during tensile deformation. The relations between lamellar colony size, lamellar spacing and strength also accord with Hall-Petch relationship. The dislocations are piled up at the lamellar colony boundaries and lamellar interfaces during the tensile deformation, so higher tensile stress for TiAl alloy with finer colony size and lamellar spacing is required to drive the dislocation movement during the tensile deformation. Also, the small lamellar spacing inhibits tans-lamellar microcracks. The microcracks are mostly inter-lamellar cracks generated by normal stress originating from dislocation pile-ups within the lamellar interfaces, and the amount of dislocations generated during tensile deformation of TiAl alloy is proportional to the lamellar spacing, so the linkage of the main crack with inter-lamellar microcracks becomes difficult for the TiAl alloy with finer lamellar spacing during tensile

deformation. By contrast, the large lamellar spacing increases the tendency of trans-lamellar microcrack and linkage of the main crack with trans-lamellar and inter-lamellar microcracks is much easier to occur, leading to the reduction in fracture resistance. The lamellar colony size and lamellar spacing decrease gradually from the lower part to the upper part of as-deposited TiAl alloy along building direction, resulting in the upper part of as-deposited TiAl alloy shows higher tensile strength. The smaller lamellar colony size is beneficial to enhance the deformation compatibility of alloy during tensile test, so the elongation is also enhanced from the lower to upper part.

Furthermore, the volume fraction ratio of α_2 phase and γ phase is the other factor influencing the tensile properties of TiAl alloys. The tensile deformation mainly concentrates on the γ phase in tensile process of the TiAl alloys, the dislocation slip of γ phase preferentially occurs on {111}<110> slip system. The γ phase belongs to tetragonal $L1_0$ structure because of the alternatively distributed stacking sequence of Ti and Al atomic planes along the <001> direction. Thus, the <110] and <101] directions of γ phase are not equivalent, forming two types of dislocation: superdislocations with Burgers vectors $\mathbf{b} = 1/2<101]$ and $1/2<11\bar{2}]$, and ordinary dislocations with Burgers vector $\mathbf{b} = 1/2<110]$. In addition, the four additional $\{111\}<11\bar{2}>$ twinning systems can be also motivated in the γ phase [28]. The α_2-Ti_3Al phase, with hexagonal ordered $D0_{19}$ structure, has only three slip systems involving the prim, basal and pyramidal planes, and its deformation is carried by superdislocations with complex core structures, decomposition and dissociation reactions involving various types of planar faults obviously make the activation of certain slip systems difficult [2]. Thus, the γ phase exhibits more ductile behavior than α_2 phase. The volume fraction of α_2 phase presented the decrease tendency from the lower part to the upper part along building direction, therefore, the elongation is also apparently enhanced from 0.28% to 0.55%. Moreover, the bottom part of the as-deposited TiAl alloy close to the substrate suffered from higher stress due to higher cooling rate, which is detrimental to the tensile properties.

The fracture morphologies can reflect the tensile properties of alloy, which are further analyzed. As mentioned above, the fracture surfaces all include trans-lamellar and inter-lamellar fracture characteristics, but the number of facets, the typical feature of inter-lamellar fracture, is fewer in the upper part, followed by the middle part, the lower part of as-deposited TiAl alloy. The inter-lamellar cracks are easy to occur for TiAl alloy with larger lamellar spacing due to the stress concentration generated by dislocation pile-ups, which is detrimental to the tensile properties. However, the trans-lamellar crack is difficult to grow. The effective tensile area reduces gradually with the amount of inter-lamellar cracks increasing, and the linkage of main cracks with inter-lamellar microcracks becomes relatively easy, finally resulting in the fracture of tensile specimen. Moreover, the secondary crack along lamellar interface after tensile can be also found in the tensile fracture surface of lower part of as-deposited TiAl alloy component. The secondary cracks propagation along the lamellar interface is the result of seeking the minimum resistance path when the main crack grows, which illustrate lamellar microstructure with larger lamellar spacing is much easier to generate inter-lamellar cracks. As a result, the lower part of as-deposited TiAl alloy shows poorer tensile properties compared with much higher deposition part of TiAl alloy fabricated by TW-PAAM.

5. Conclusions

In the present research, the Ti-48Al alloy is fabricated successfully using TW-PAAM. The microstructure and mechanical properties of as-deposited TiAl alloy at different deposition locations are analyzed in detail. The results can be concluded as follows:

1. The buildup TiAl alloy exhibits alternatively distributed layer-like microstructure composed of dendritic grain region and fully lamellar colony region. The dendritic grain region consists of lamellar microstructure with interdendritic γ phase, and there are also some feathery structure, Widmanstätten laths and discontinuous coarsening of lamellae observed in the fully lamellar colony region.
2. The buildup alloy contains α_2 and γ phase. The content of α_2 phase, lamellar colony size and lamellar spacing all exhibit the tendency of decreasing from the lower to the upper part.
3. The microhardness distribution presents approximate periodicity along the building direction due to the alternatively distributed layer-like microstructure, the mean microhardness value is higher in the dendritic grain region (342HV) than that in the fully lamellar colony region (315HV).
4. The tensile strength and elongation of as-deposited TiAl alloy significantly depend on the height of deposition location. The upper part of as-deposited TiAl alloy exhibits the maximum UTS and elongation (419.3 MPa and 0.55%), followed by the middle part (367.4 MPa and 0.46%). However, the UTS and elongation in the lower part drop respectively to 298.6 MPa, 0.28%, which are mainly attributed to microstructure characteristics variation, including the lamellar colony size, lamellar spacing, the amount of α_2 phase, etc.

CRediT authorship contribution statement

Lin Wang: designed and conducted the study and wrote the manuscript. **Yuelong Zhang:** helped to fabricate the TiAl alloy. Xueming Hua, Writing – review & editing, is the leader of research group and helped to review the manuscript. Chen Shen, Formal analysis, Writing – review & editing, helped to analyze data and review the manuscript. **Fang Li:** helped to understand the experimental results. **Ye Huang:** helped to draw the figures. **Yuhan Ding:** helped to perform experiment tests.

Declaration of competing interest

The authors declare that they have no known competing financial interests or personal relationships that could have appeared to influence the work reported in this paper.

Acknowledgments

The authors gratefully acknowledge financial support from Science and Technology Commission of Shanghai Municipality (STCSM, Funding No. 19511106400, “Sailing Program” No. 19YF1422700) and National Natural Science Foundation of China (NSFC, Funding No. 51901136). The authors would also like to thank Xiaomin Li in the Instrumental Analysis Center of Shanghai Jiao Tong University for helping in instrumental operation.

References

[1] X. Wu, Review of alloy and process development of TiAl alloys, Intermetallics 14 (10–11) (2006) 1114–1122.
[2] K. Kothari, R. Radhakrishnan, N.M. Wereley, Advances in gamma titanium aluminides and their manufacturing techniques, Prog. Aero. Sci. 55 (2012) 1–16.
[3] H. Clemens, S. Mayer, Design, processing, microstructure, properties, and applications of advanced intermetallic TiAl alloys, Adv. Eng. Mater. 15 (4) (2013) 191–215.
[4] B.P. Bewlay, S. Nag, A. Suzuki, M.J. Weimer, TiAl alloys in commercial aircraft engines, Mater. A. T. High. Temp. 33 (4–5) (2016) 549–559.
[5] A. Couret, T. Voisin, M. Thomas, J.-P. Monchoux, Development of a TiAl alloy by spark plasma sintering, JOM (J. Occup. Med.) 69 (12) (2017) 2576–2582.
[6] H.P. Tang, G.Y. Yang, W.P. Jia, W.W. He, S.L. Lu, M. Qian, Additive manufacturing of a high niobium-containing titanium aluminide alloy by selective electron beam melting, Mater. Sci. Eng., A 636 (2015) 103–107.
[7] Y. Ma, D. Cuiuri, H. Li, Z. Pan, C. Shen, The effect of postproduction heat treatment on γ-TiAl alloys produced by the GTAW-based additive manufacturing process, Mater. Sci. Eng., A 657 (2016) 86–95.
[8] ≤Anisotropy and Heterogeneity of Microstructure and Mechanical Properties in Metal Additive Manufacturing A Critical review.Pdf>.
[9] B.T. Wu, Z.X. Pan, D.H. Ding, D. Cuiuri, H.J. Li, J. Xu, J. Norrish, A review of the wire arc additive manufacturing of metals: properties, defects and quality improvement, J. Manuf. Process. 35 (2018) 127–139.

[10] V.K. Balla, M. Das, A. Mohammad, A.M. Al-Ahmari, Additive manufacturing of γ-TiAl: processing, microstructure, and Properties, Adv. Eng. Mater. 18 (7) (2016) 1208–1215.
[11] W. Li, J. Liu, Y. Zhou, S. Li, S. Wen, Q. Wei, C. Yan, Y. Shi, Effect of laser scanning speed on a Ti-45Al-2Cr-5Nb alloy processed by selective laser melting: microstructure, phase and mechanical properties, J. Alloys Compd. 688 (2016) 626–636.
[12] A.R.C. Sharman, J.I. Hughes, K. Ridgway, Characterisation of titanium aluminide components manufactured by laser metal deposition, Intermetallics 93 (2018) 89–92.
[13] T.C. Dzogbewu, Additive manufacturing of TiAl-based alloys, Manuf. Rev. 7 (2020).
[14] J. Zhou, H. Li, Y. Yu, Y. Li, Y. Qian, K. Firouzian, F. Lin, Research on aluminum component change and phase transformation of TiAl-based alloy in electron beam selective melting process under multiple scan, Intermetallics 113 (2019).
[15] Y. Chen, H. Yue, X. Wang, S. Xiao, F. Kong, X. Cheng, H. Peng, Selective electron beam melting of TiAl alloy: microstructure evolution, phase transformation and microhardness, Mater. Char. 142 (2018) 584–592.
[16] G. Baudana, S. Biamino, D. Ugues, M. Lombardi, P. Fino, M. Pavese, C. Badini, Titanium aluminides for aerospace and automotive applications processed by electron beam melting: contribution of politecnico di Torino, Met. Powder Rep. 71 (3) (2016) 193–199.
[17] H. Yue, Y. Chen, X. Wang, S. Xiao, F. Kong, Microstructure, texture and tensile properties of Ti-47Al-2Cr-2Nb alloy produced by selective electron beam melting, J. Alloys Compd. 766 (2018) 450–459.
[18] J. Schwerdtfeger, C. Körner, Selective electron beam melting of Ti–48Al–2Nb–2Cr: microstructure and aluminium loss, Intermetallics 49 (2014) 29–35.
[19] C. Shen, K.-D. Liss, M. Reid, Z. Pan, Y. Ma, X. Li, H. Li, In-situ neutron diffraction characterization on the phase evolution of γ-TiAl alloy during the wire-arc additive manufacturing process, J. Alloys Compd. 778 (2019) 280–287.
[20] Y. Ma, D. Cuiuri, N. Hoye, H. Li, Z. Pan, The effect of location on the microstructure and mechanical properties of titanium aluminides produced by additive layer manufacturing using in-situ alloying and gas tungsten arc welding, Mater. Sci. Eng., A 631 (2015) 230–240.
[21] C. Shen, Z.X. Pan, D. Cuiuri, B.S. Dong, H.J. Li, In-depth study of the mechanical properties for Fe3Al based iron aluminide fabricated using the wire-arc additive manufacturing process, Mater. Sci. Eng. A-Struct. Mater. Prop. Microstruct. Process. 669 (2016) 118–126.
[22] C. Shen, M. Reid, K.D. Liss, X.M. Hua, Z.X. Pan, G. Mou, Y. Huang, H.J. Li, In-situ neutron diffraction study on the high temperature thermal phase evolution of wire-arc additively manufactured Ni53Ti47 binary alloy, J. Alloys Compd. 843 (2020) 18.
[23] C. Shen, K.-D. Liss, M. Reid, Z. Pan, X. Hua, F. Li, G. Mou, Y. Huang, Y. Zhu, H. Li, Fabrication of FeNi intermetallic using the wire-arc additive manufacturing process: a feasibility and neutron diffraction phase characterization study, J. Manuf. Process. 57 (2020) 691–699.
[24] ≤2018_Book_TransactionsOnIntelligentWeldi.pdf>.
[25] C.S. Wu, L. Wang, W.J. Ren, X.Y. Zhang, Plasma arc welding: process, sensing, control and modeling, J. Manuf. Process. 16 (1) (2014) 74–85.
[26] X.W. Bai, P. Colegrove, J.L. Ding, X.M. Zhou, C.L. Diao, P. Bridgeman, J. R. Honnige, H.O. Zhang, S. Williams, Numerical analysis of heat transfer and fluid flow in multilayer deposition of PAW-based wire and arc additive manufacturing, Int. J. Heat Mass Tran. 124 (2018) 504–516.
[27] Y. Wu, S. Zhang, X. Cheng, H. Wang, Investigation on solid-state phase transformation in a Ti-47Al-2Cr-2V alloy due to thermal cycling during laser additive manufacturing process, J. Alloys Compd. 799 (2019) 325–333.
[28] X. Zhang, C. Li, M. Zheng, Z. Ye, X. Yang, J. Gu, Anisotropic tensile behavior of Ti-47Al-2Cr-2Nb alloy fabricated by direct laser deposition, Additive Manufacturing 32 (2020).
[29] M. Todai, T. Nakano, T. Liu, H.Y. Yasuda, K. Hagihara, K. Cho, M. Ueda, M. Takeyama, Effect of building direction on the microstructure and tensile properties of Ti-48Al-2Cr-2Nb alloy additively manufactured by electron beam melting, Additive Manufacturing 13 (2017) 61–70.
[30] L. Wang, D.Q. Sun, H.M. Li, C.J. Shen, Effects of postweld heat treatment on microstructure and properties of laser-welded Ti-24Al-15Nb alloy joint, J. Mater. Eng. Perform. 28 (11) (2019) 6827–6835.
[31] S.R. Dey, A. Hazotte, E. Bouzy, Crystallography and phase transformation mechanisms in TiAl-based alloys – a synthesis, Intermetallics 17 (12) (2009) 1052–1064.
[32] W. Li, J. Liu, S. Wen, Q. Wei, C. Yan, Y. Shi, Crystal orientation, crystallographic texture and phase evolution in the Ti–45Al–2Cr–5Nb alloy processed by selective laser melting, Mater. Char. 113 (2016) 125–133.
[33] Q. Wang, H. Ding, H. Zhang, R. Chen, J. Guo, H. Fu, Variations of microstructure and tensile property of γ-TiAl alloys with 0–0.5at% C additives, Mater. Sci. Eng., A 700 (2017) 198–208.
[34] Y. Chen, H. Niu, F. Kong, S. Xiao, Microstructure and fracture toughness of a β phase containing TiAl alloy, Intermetallics 19 (10) (2011) 1405–1410.
[35] M.S. Dahar, S.M. Seifi, B.P. Bewlay, J.J. Lewandowski, Effects of test orientation on fracture and fatigue crack growth behavior of third generation as-cast Ti–48Al–2Nb–2Cr, Intermetallics 57 (2015) 73–82.
[36] Y. Chen, H. Yue, X. Wang, Microstructure, texture and tensile property as a function of scanning speed of Ti-47Al-2Cr-2Nb alloy fabricated by selective electron beam melting, Mater. Sci. Eng., A 713 (2018) 195–205.
[37] M. Charpentier, A. Hazotte, D. Daloz, Lamellar transformation in near-γ TiAl alloys—quantitative analysis of kinetics and microstructure, Mater. Sci. Eng., A 491 (1) (2008) 321–330.
[38] D. Hu, R.R. Botten, Phase transformations in some TiAl-based alloys, Intermetallics 10 (7) (2002) 701–715.
[39] J. Yang, J.N. Wang, Y. Wang, Q. Xia, Refining grain size of a TiAl alloy by cyclic heat treatment through discontinuous coarsening, Intermetallics 11 (9) (2003) 971–974.
[40] W. Li, J. Liu, Y. Zhou, S. Wen, Q. Wei, C. Yan, Y. Shi, Effect of substrate preheating on the texture, phase and nanohardness of a Ti–45Al–2Cr–5Nb alloy processed by selective laser melting, Scripta Mater. 118 (2016) 13–18.
[41] J. Fan, X. Li, Y. Su, J. Guo, H. Fu, The microstructure parameters and microhardness of directionally solidified Ti–43Al–3Si alloy, J. Alloys Compd. 506 (2) (2010) 593–599.
[42] H. Wang, D. Zhu, C. Zou, Z. Wei, Evolution of the microstructure and nanohardness of Ti–48at.%Al alloy solidified under high pressure, Mater. Des. 34 (2012) 488–493.
[43] K.S. Chan, Y.W. Kim, Effects of lamellae spacing and colony size on the fracture resistance of a fully-lamellar TiAl alloy, Acta Metall. Mater. 43 (2) (1995) 439–451.